ORNL/TM--9193

DE84 017633

Fusion Energy Division

MONTE CARLO STUDIES OF TRANSPORT IN STELLARATORS

R. H. Fowler

Computer Sciences

J. A. Rome and J. F. Lyon

Fusion Energy Division

Date Published - August 1984

NOTICE This document contains information of a preliminary nature. It is subject to revision or correction and therefore does not represent a final report.

Prepared by the
OAK RIDGE NATIONAL LABORATORY
Oak Ridge, Tennessee 37831
operated by
Martin Marietta Energy Systems, Inc.
for the
U.S. DEPARTMENT OF ENERGY
under Contract No. DE-AC05-84OR21400

CONTENTS

ACKNOWLEDGMENTS v

ABSTRACT vii

1. INTRODUCTION 1

2. DRIFT EQUATIONS IN MAGNETIC COORDINATES AT FINITE BETA 1

3. CALCULATION OF B IN MAGNETIC COORDINATES 3

4. METHODS FOR COMPUTING D 4

   4.1. METHOD 1: DISPERSION 4
   4.2. METHOD 2: ENSEMBLE AVERAGE WITH $\Delta t \rightarrow \infty$ 5
   4.3. METHOD 3: PITCH ANGLE SCATTERING ONLY 6

5. LOSS RATE CALCULATIONS 7

6. TOKAMAK BENCHMARK CASE 8

7. RADIAL ELECTRIC FIELD EFFECTS 11

8. SUMMARY 16

REFERENCES 17

ABSTRACT

Transport is studied in toroidal geometry by integrating the guiding-center equations in magnetic coordinates and simulating collisions with a Monte Carlo collision operator. The effects of the ambipolar electric field on diffusion losses are determined for model magnetic fields and the correct magnetic field of the Advanced Toroidal Facility (ATF-1) stellarator. Comparisons are made of the computed diffusion coefficients and the theoretically predicted values.

1. INTRODUCTION

In a number of recent papers,[1-3] Monte Carlo methods have been used to investigate transport properties in nonaxisymmetric tori. Because of the complex geometry, previous authors have generally used simple magnetic field models. The purpose of the present work is to investigate the effects of radial electric fields on diffusion losses in stellarators using realistic magnetic fields. For the vacuum cases, these fields are determined from the Biot-Savart law using multifilament models for the coil sets. Alternatively, the output from a three-dimensional (3-D) equilibrium code is employed.

The Monte Carlo procedures in this paper closely parallel those developed by Boozer and Kuo-Petravic[1] and by Wobig.[3] In general, particles are started at random locations and pitch angles on a given flux surface. The guiding-center motions are computed in magnetic coordinates, and at each integration step, the particles are scattered in pitch angle and energy using the appropriate Monte Carlo operators. Relevant information is recorded for later calculations of properties of interest, such as loss rates and diffusion coefficients. In the work reported here only thermal ion collisions are considered; however, the methods are applicable to electrons.

In Sect. 2, the guiding-center equations in magnetic coordinates, valid at finite beta, are given. The procedures for computing the magnetic fields are described in Sect. 3. The methods for computing diffusion coefficients and the technique for determining particle flux to the wall are given in Sects. 4 and 5, respectively. In Sect. 6 the results of a benchmark tokamak case are given. Finally, in Sect. 7 the Monte Carlo results for an idealized stellarator case are compared with analytic theory. Also given are the results for the vacuum field and finite-beta cases valid for the Advanced Toroidal Facility (ATF-1) stellarator.

2. DRIFT EQUATIONS IN MAGNETIC COORDINATES AT FINITE BETA

Following orbits in magnetic coordinates reveals the true nature of the orbit since the slow motion across the field lines is separated from the fast motion along the field lines. This system is natural for representing quantities such as density, temperature, and electric potential that are normally functions of the toroidal flux. It also has the computational advantage of requiring only information about the magnitude of **B**, not the vector components, while tracing orbits.

The drift orbit equations in magnetic coordinates most often used are only valid for curl-free magnetic fields. The orbit equations given below are derived in magnetic coordinates using Boozer's[4] Hamiltonian formulation and are valid for both vacuum and finite-beta fields. These equations in ψ, ρ_c, θ, and ϕ coordinates are

$$\dot{\psi} = \frac{\dot{P}_\theta g - \dot{P}_\phi I}{\gamma} \quad , \tag{1}$$

$$\dot{\rho}_c = \frac{-(\rho_c g' - \iota)\dot{P}_\theta + (\rho_c I' + 1)\dot{P}_\phi}{\gamma} \quad , \tag{2}$$

$$\dot{\theta} = \left(\delta \frac{\partial B}{\partial \psi} + e \frac{\partial \Phi}{\partial \psi}\right) \frac{\partial \psi}{\partial P_\theta} + \frac{e^2 B^2}{m} \rho_c \frac{\partial \rho_c}{\partial P_\theta} \quad , \tag{3}$$

$$\dot{\phi} = \left(\delta \frac{\partial B}{\partial \psi} + e \frac{\partial \Phi}{\partial \psi}\right) \frac{\partial \psi}{\partial P_\phi} + \frac{e^2 B^2}{m} \rho_c \frac{\partial \rho_c}{\partial P_\phi} \quad , \tag{4}$$

where $2\pi\psi$ is the toroidal flux, $\rho_c = mv_\parallel/eB$, and θ and ϕ are the periodic poloidal and toroidal angles, respectively. The toroidal current within a flux surface is $I(\psi)/(2 \times 10^{-7})$ A, and the poloidal current outside a flux surface is $g(\psi)/(2 \times 10^{-7})$ A. The functions $I(\psi)$, $g(\psi)$, and the rotational transform $\iota(\psi)$ are computed on a ψ mesh by evaluating the appropriate line integrals of the magnetic field **B**. The electrostatic potential in this work is taken to be of the form

$$\Phi = \Phi_0(1 - \psi/\psi_e) \quad , \tag{5}$$

where ψ_e specifies the plasma edge.

The functions γ and δ are defined by

$$\gamma = e\left[g(\rho_c I' + 1) - I(\rho_c g' - \iota)\right] \quad , \tag{6}$$

$$\delta = \frac{e^2 \rho_c^2 B}{m} + \mu \quad . \tag{7}$$

The canonical momenta are given by

$$P_\theta = -\delta \frac{\partial B}{\partial \theta} \quad , \tag{8}$$

$$P_\phi = -\delta \frac{\partial B}{\partial \phi} \quad . \tag{9}$$

The derivatives of ψ and ρ_c with respect to the momenta are

$$\frac{\partial \psi}{\partial P_\theta} = \frac{g}{\gamma} \quad , \tag{10}$$

$$\frac{\partial \rho_c}{\partial P_\theta} = -\frac{(\rho_c g' - \iota)}{\gamma} \quad , \tag{11}$$

$$\frac{\partial \psi}{\partial P_\phi} = -\frac{I}{\gamma} \quad , \tag{12}$$

$$\frac{\partial \rho_c}{\partial P_\phi} = \frac{(I'\rho_c + 1)}{\gamma} \quad . \tag{13}$$

The pitch angle and energy scattering operators, which may be applied after each time step, are similar to those given in ref. 1, but with modifications to allow for collisions between unlike particles.

A number of integration techniques have been tested for these equations with energy conservation serving as an accuracy check. The most suitable integrator for collisionless orbits is STEP,[5] based on the Adams method. However, in the cases with collisions, an integrator based on the Burlirsch and Stoer[6] extrapolation method was chosen because of less overhead in restarting the integrations.

3. CALCULATION OF B IN MAGNETIC COORDINATES

In this magnetic coordinate system, B is represented by

$$B = \sum_{n,m} A_{nm}(\psi) \cos(n\phi - m\theta) \quad .$$

To determine A_{nm} on a given flux surface, the values of B and χ, where

$$\chi = g(\psi)\phi + I(\psi)\theta = \int \mathbf{B} \cdot d\ell \quad ,$$

are obtained along a field line, and fast Fourier transforms are applied as described in ref. 7. During this process the functions $g(\psi)$, $I(\psi)$, and $\iota(\psi)$ are also obtained.

The magnetic field $B(\chi)$ is determined in two ways for studies of transport in the ATF-1 stellarator. For the vacuum case, the helical coil set is modeled with straight filamentary segments as a basis of the Biot-Savart law. Four to eight filamentary windings represent each of the two helical coils. As many as 216 segments around the torus are used for each filamentary winding. The circular vertical field coils are modeled by circular filaments. For the finite-beta case, the equilibrium from a 3-D Chodura-Schlüter code[8] is used. The equilibrium code employs similar vacuum fields. In order to vectorize the calculation of B for the CRAY computer, least-squares fits of the functions of ψ are done with third- or fourth-degree polynomials.

4. METHODS FOR COMPUTING D

The determination of local plasma diffusion coefficients for realistic situations is inherently difficult. At the microscopic level, diffusion is due to random motion caused by collisions. The time for following this motion should be long compared to the orbit time, preferably a number of 90° collision times. However, for a finite-size system this time should not be so long that the diffusion distance is comparable to the dimensions of the system. The difficulty arises when many orbits have large deviations from their birth flux surfaces, that is, when the orbits are nonlocal. To ensure that the calculation of the diffusion coefficient D is correct, a number of approaches and precautions have been taken.

First, to have a "quiet" start, the collisionless motion of groups of particles is followed for several orbit times. Initially, the particles are on the same flux surface ψ_0 but have a uniform random distribution in θ, ϕ, and pitch angle. Normally, $\psi_0 = 0.25\psi_e$, and the energy distribution is generally chosen from a Maxwellian distribution. Particles that are lost during this initial phase are rejected and replaced. Once a satisfactory group of N particles (usually $N = 64$) is obtained, collisions are introduced. The starting positions of these particles are the coordinates at the termination of the collisionless motion. The group of particles is followed for several 90° scattering times but ideally for a period much less than the confinement time. If a particle is lost (ψ becomes greater than ψ_e), it is replaced by a new particle at ψ_0 with the other coordinates as described above. This maintains a constant number of particles in the system and is useful for computing loss rates that are discussed later. After a statistically sufficient number of groups of particles are followed, D is computed from the recorded information as described below.

4.1. METHOD 1: DISPERSION

Starting with the diffusion equation for the particle distribution, it is easily shown that

$$D = \frac{\langle \psi^2 \rangle - \langle \psi \rangle^2}{2t} = \frac{\text{dispersion}}{2t} , \tag{14}$$

where the brackets imply ensemble averages at time t. The form of the dispersion when D has a valid definition is $2Dt + C$, a straight line with D as the slope. This method is similar to the one used in molecular dynamics studies of classical fluids where D is found from the slope of the mean square displacement.

In the actual calculation, ψ is replaced by ψ/ψ_e and D is converted to spatial units by

$$D(\text{cm}^2/\text{s}) = \frac{\psi_e}{4\psi_0} a^2 D(\psi_0) , \tag{15}$$

where a is the minor radius of the system in centimeters.

4.2 METHOD 2: ENSEMBLE AVERAGE WITH $\Delta t \rightarrow \infty$

For a given $\Delta t = t_j - t_{j-1}$ = constant and for each particle k, let D_{jk} be defined as

$$D_{jk} = \frac{1}{2\Delta t}\left[\psi(t_j) - \psi(t_{j-1})\right]^2 . \tag{16}$$

Therefore, for N particles and J constant time intervals, let

$$D(\Delta t) = \frac{1}{N}\sum_{k=1}^{N}\frac{1}{J}\sum_{j=1}^{J} D_{jk} . \tag{17}$$

This is the method described in ref. 1 with Δt corresponding to one 90° scattering time. Thus, the above sums are over all particles k and over all t_j, but with fixed Δt. Strictly speaking,

$$D = \lim_{\Delta t \rightarrow \infty} \frac{[\psi(t + \Delta t) - \psi(t)]^2}{2\Delta t} . \tag{18}$$

Therefore, D at ψ_0, is obtained by plotting $D(\Delta t)$ versus Δt^{-1} and extrapolating to $\Delta t \rightarrow \infty$. As a check of the accuracy of this procedure,[1] for each $D(\Delta t)$ a plot is made of the actual D_j/D distribution versus the expected chi-square distribution:

$$P(D_j) = \left(\frac{2\pi D_j}{D}\right)^{-1/2} \exp\left(\frac{-D_j}{2D}\right) . \tag{19}$$

The D_j/D distribution is divided into intervals that should each have 5% of the distribution according to $P(D_j)$. The deviation from the expected value is an indication of the error in the Monte Carlo simulation.

Figure 1 gives a comparison of the above methods for a stellarator with a model field

$$B = B_0\left[1 - \epsilon_a(\psi/\psi_e)^{1/2}\cos\theta - \delta_a(\psi/\psi_e)^{\ell/2}\sin(\ell\theta - m\phi)\right] . \tag{20}$$

For this case 256 ions with initial kinetic energy of 1 keV were followed for 3 ms (about 5 collision times). The plasma temperature and density were constants of 3×10^{13} cm^{-3} and 1 keV, respectively. The field parameters were $B_0 = 5$ T, $\epsilon_a = 0.10$, $\delta_a = 0.30$, $\Phi_0 = 4$ kV, $\ell = 1$, and $m = 12$. The chi-square plot is the distribution of D_j computed with the largest Δt for this case. The maximum and minimum numbers of D_j in any interval are, respectively, approximately 20 and 6, compared with the expected value of 12.8. From the standard deviation σ, the relative error ($\sigma/D_j\sqrt{N}$) of 14% for the mean D_j was obtained for this distribution.

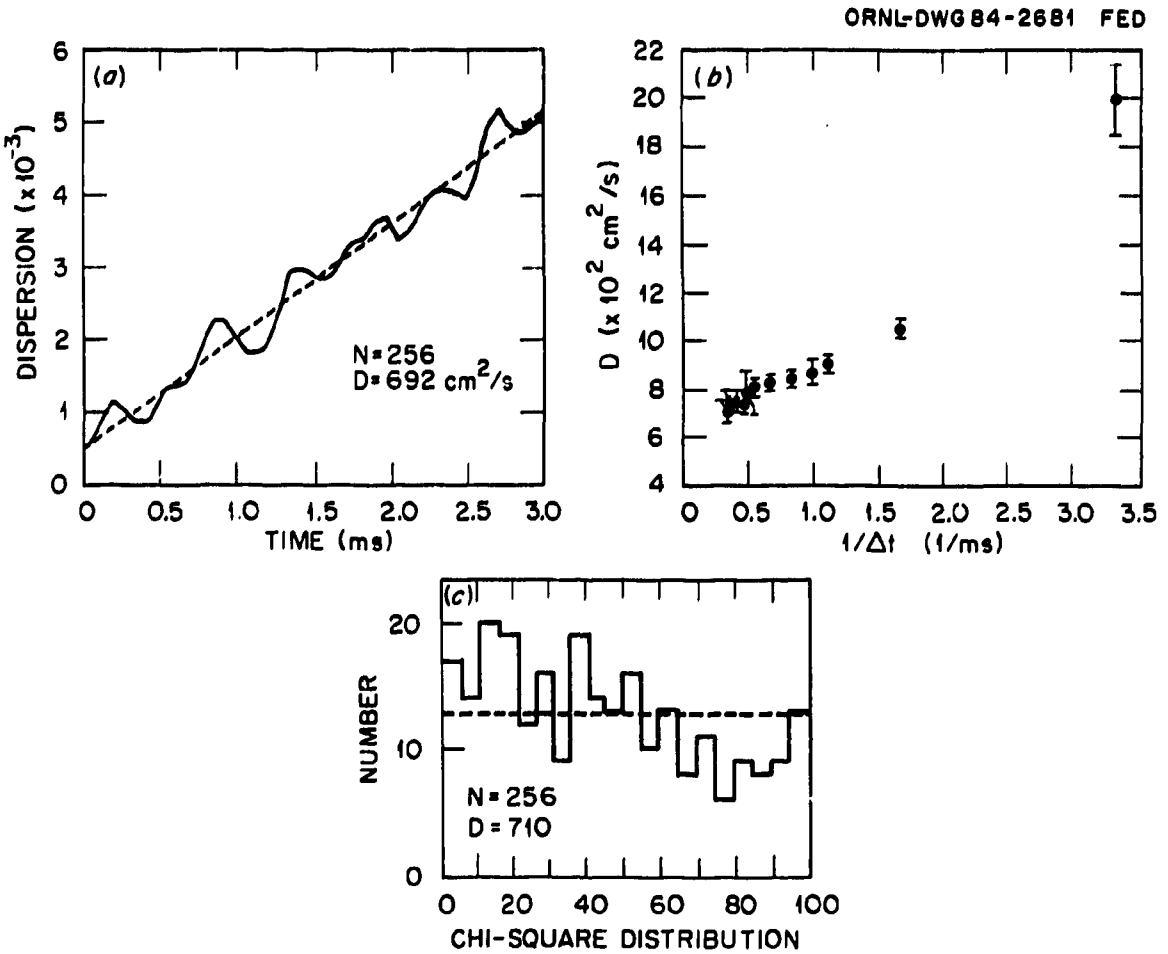

Fig. 1. The diffusion coefficient computed by two methods: (a) dispersion curve and (b) $D(\Delta t)$. The chi-square distribution for the largest Δt is given in (c).

4.3. METHOD 3: PITCH ANGLE SCATTERING ONLY

A third approach is to have only pitch angle scattering. In this method the particles are all started with the same energy. The statistics for these cases are better than those with energy scattering; however, a number of runs at different energies must be done in order to average over a Maxwellian distribution.

The agreement of these methods is good for cases when the diffusion process is a dominant feature of the system, that is, when there is not a large prompt loss of particles resulting from nonrandom motion. When there is a large, rapid, and direct particle loss, local diffusion (as defined above) no longer has meaning.

5. LOSS RATE CALCULATIONS

For those situations when local diffusion is not a dominant feature of the system, the Monte Carlo procedures are still useful for computing particle and energy fluxes to the outer flux surface. The cumulative rate of energy loss at time t is defined as

$$P_L(t) = \frac{1}{N\langle E_0\rangle t} \sum_j p_{Lj}\Delta t \ . \tag{21}$$

where $p_{Lj}\Delta t$ is the energy lost during the time interval, $\Delta t = t_j - t_{j-1}$, and $N\langle E_0\rangle$ is the mean initial energy of the N particles of the system. The cumulative particle loss rate is defined similarly. Lost particles are replaced as described above. The flux of particles to ψ_e and the distribution function $f(t,\psi,\eta)$, with $\eta = v_\parallel/v$, are monitored until steady state is reached. The energy confinement time is found from

$$\tau_E = \frac{3}{2} \frac{\langle T\rangle}{\langle E_L/t_L\rangle} \ , \tag{22}$$

where $\langle T\rangle$ is the volume-averaged temperature and $\langle E_L/t_L\rangle$ is the average power loss. A loss rate calculation is illustrated in Fig. 2 for the ATF-1 vacuum field with no electric potential. Figure 2(c) is the

$$\ln\left[\sum \frac{\Delta t}{NtE^{1/2}\Delta E}\right] ,$$

where $\sum \Delta t/Nt$ is the fraction of time the N particles spent in the energy bin $E \pm \Delta E/2$ with $\Delta E = 0.25$ keV. The dashed line,

$$\ln\left[\frac{2}{\sqrt{\pi}} \frac{1}{(kT)^{3/2}}\right] - E/kT \ ,$$

is obtained from the expected Maxwellian distribution. In this case, the temperature and density were constant with values of 1 keV and 3×10^{13} cm^{-3}, respectively. The magnetic field at the center was 2 T.

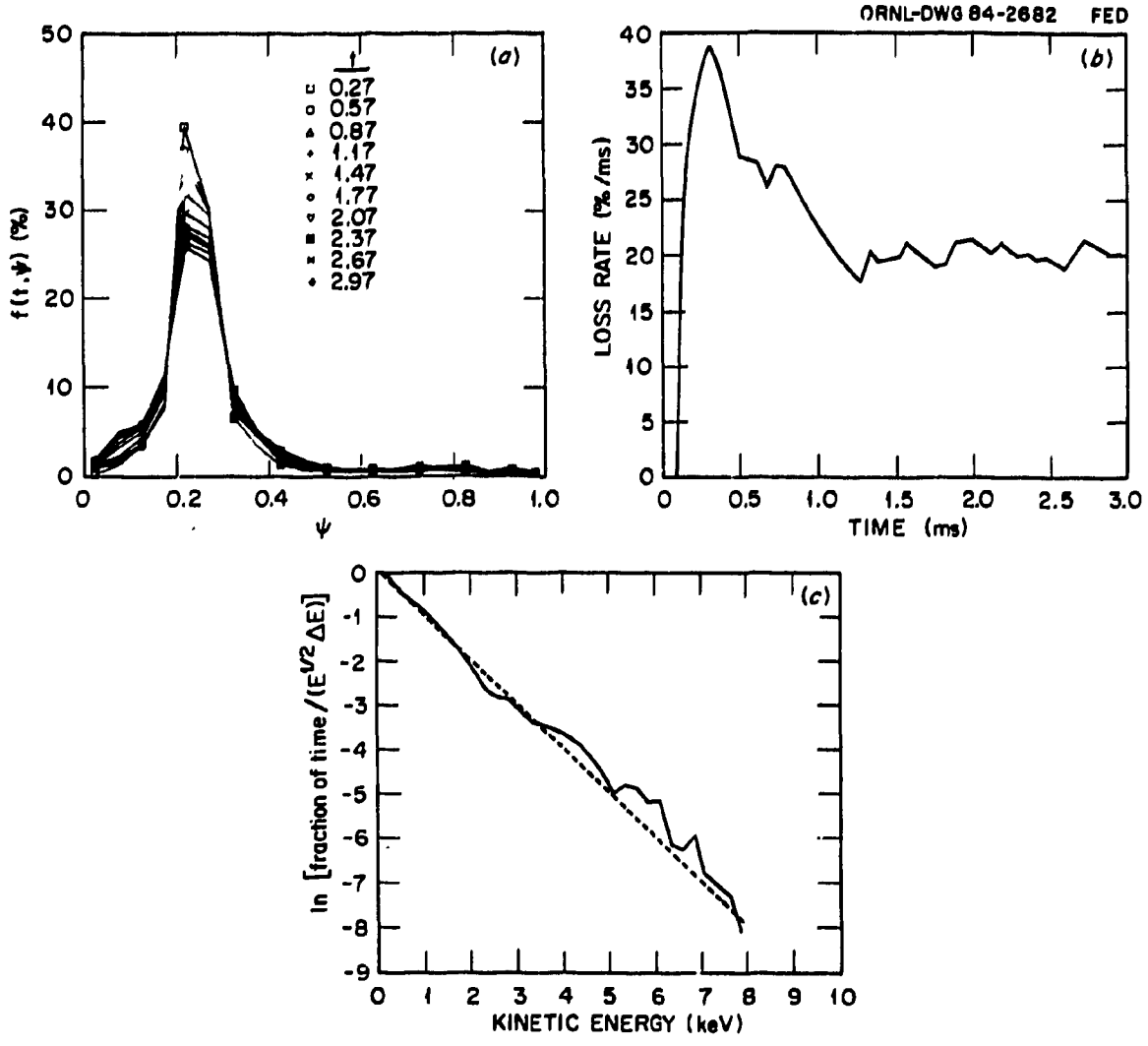

Fig. 2. Ions are started randomly on the flux surface $\psi/\psi_e = 0.25$. Shown at various times are (a) the distribution function $f(t,\psi)$, (b) the particle flux to the wall, and (c) the final energy distribution of the particles where the dashed line is obtained from the expected Maxwellian distribution.

6. TOKAMAK BENCHMARK CASE

The numerical calculation of diffusion coefficients has been benchmarked with the neoclassical theory of Hinton, Rosenbluth, and Hazeltine[9,10] for a tokamak case. The analytic expressions used for comparison are given by

$$D = \epsilon^{1/2}\nu \left[\frac{\rho B_t}{B_p} \right]^2 k_\parallel , \tag{23}$$

$$k_{\parallel} = 1.04 \left(\frac{1}{1 + 2.01\nu_*^{1/2} + 1.53\nu_*} + \frac{0.518\epsilon^3\nu_*}{1 + 0.89\epsilon^{3/2}\nu_*} \right) , \tag{24}$$

$$\nu_* = \frac{\nu}{\epsilon\omega_b} , \tag{25}$$

$$\omega_b = 9.78 \times 10^5 \frac{\epsilon^{1/2}t}{R_o \text{ (cm)}} \sqrt{T_i \text{ (eV)}} , \tag{26}$$

$$t = \frac{1}{q} = \frac{B_p}{\epsilon B_t} , \tag{27}$$

$$\rho = \frac{144}{B_t \text{ (g)}} \sqrt{\frac{A_i T_i \text{ (eV)}}{Z_i}} , \tag{28}$$

$$\epsilon = \frac{r}{R_o} . \tag{29}$$

The collision frequency ν is taken to be

$$\nu_{ii} = 6.77 \times 10^{-8} \frac{Z_i^4 n_i \ln \Lambda_{ii}}{T_i^{3/2} \sqrt{2A_i}} \tag{30}$$

and

$$\ln \Lambda_{ii} = 23 - \ln \left(\frac{Z_i^2}{T_i^{3/2}} \sqrt{2n_i Z_i^2} \right) . \tag{31}$$

For this case, the magnetic field was modeled by

$$B = B_t \left[1 - \epsilon_a (\psi/\psi_e)^{1/2} \cos \theta \right] , \tag{32}$$

where ϵ_a is the inverse edge aspect ratio.

The particles were started about $\psi/\psi_e = r^2/a^2 = 0.25$ with a Maxwellian energy distribution. The collisions included both pitch angle and energy scattering. Table 1 gives the parameters used. The density n_i was varied to produce values of $0.1 \leq \nu_* \leq 100$. The numerical diffusion coefficients were obtained from the slopes of the dispersion curves. The numerical results and analytic formula agree as shown in Fig. 3.

In addition to this benchmark case, the code has been successfully benchmarked against the Garching Monte Carlo codes.[2]

Table 1. Parameters used for tokamak benchmark case

Parameter	Value
A_i	1
Z_i	1
ϵ	0.05
R_o (cm)	200
a (cm)	20
B_t (T)	2
κ	0.50
T_i, T_e (keV)	1

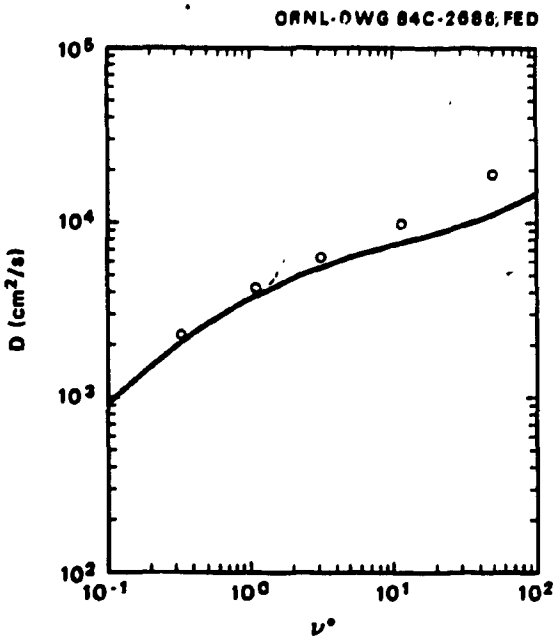

Fig. 3. The diffusion coefficient for a tokamak. The circles are the Monte Carlo results, and the curve is obtained from the analytic formula.

7. RADIAL ELECTRIC FIELD EFFECTS

The particle fluxes in stellarators are not intrinsically ambipolar, and a radial electric field develops to ensure quasi-neutrality. The effects of such electric fields have been studied for a model magnetic field and the correct magnetic fields of ATF-1, for both the vacuum and finite-beta cases.

First, collisionless orbit confinement is studied by following groups of 100 monoenergetic particles that are started at random locations and pitch angles throughout the plasma. The orbits are followed for typically 5–10 toroidal transits or until they pass through the outermost flux surface. The collisionless orbit confinement is drastically improved with radial potentials on the order of the particle's energy, basically independent of the sign of the potential. This is illustrated in Fig. 4. Plotted is the weighted

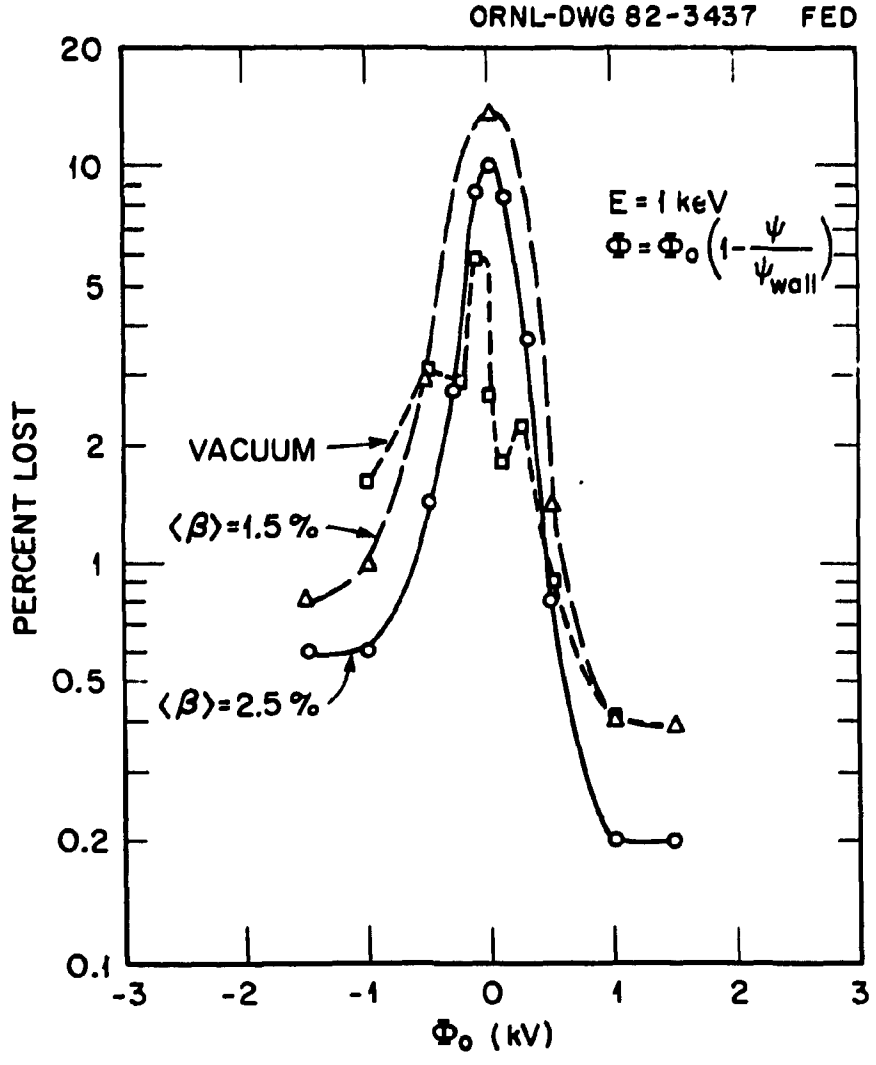

Fig. 4. Loss of 1-keV protons vs radial potential for vacuum and finite-beta fields.

percentage lost versus the potential given by Eq. (5). Curves are shown for three ATF-1 cases: vacuum, $\langle\beta\rangle = 1.5\%$, and $\langle\beta\rangle = 2.5\%$. Initially, the shift of the flux surfaces increases the particle losses by about a factor of 2 because of the increase in the variation of $\int d\ell/B$ and the resultant increase in the radial drift of the helically trapped particles. However, further increases in β improve particle confinement probably because of the increasing diamagnetic well. The effect of β on orbit topology is illustrated in Fig. 5 for a helically trapped particle.

The reason that the electric field is so effective at closing the loss regions is that the radial drift velocities of the helically trapped ions are slow compared to the $\mathbf{E} \times \mathbf{B}$ velocity, even for relatively small potentials. This is illustrated in Fig. 6, which shows a

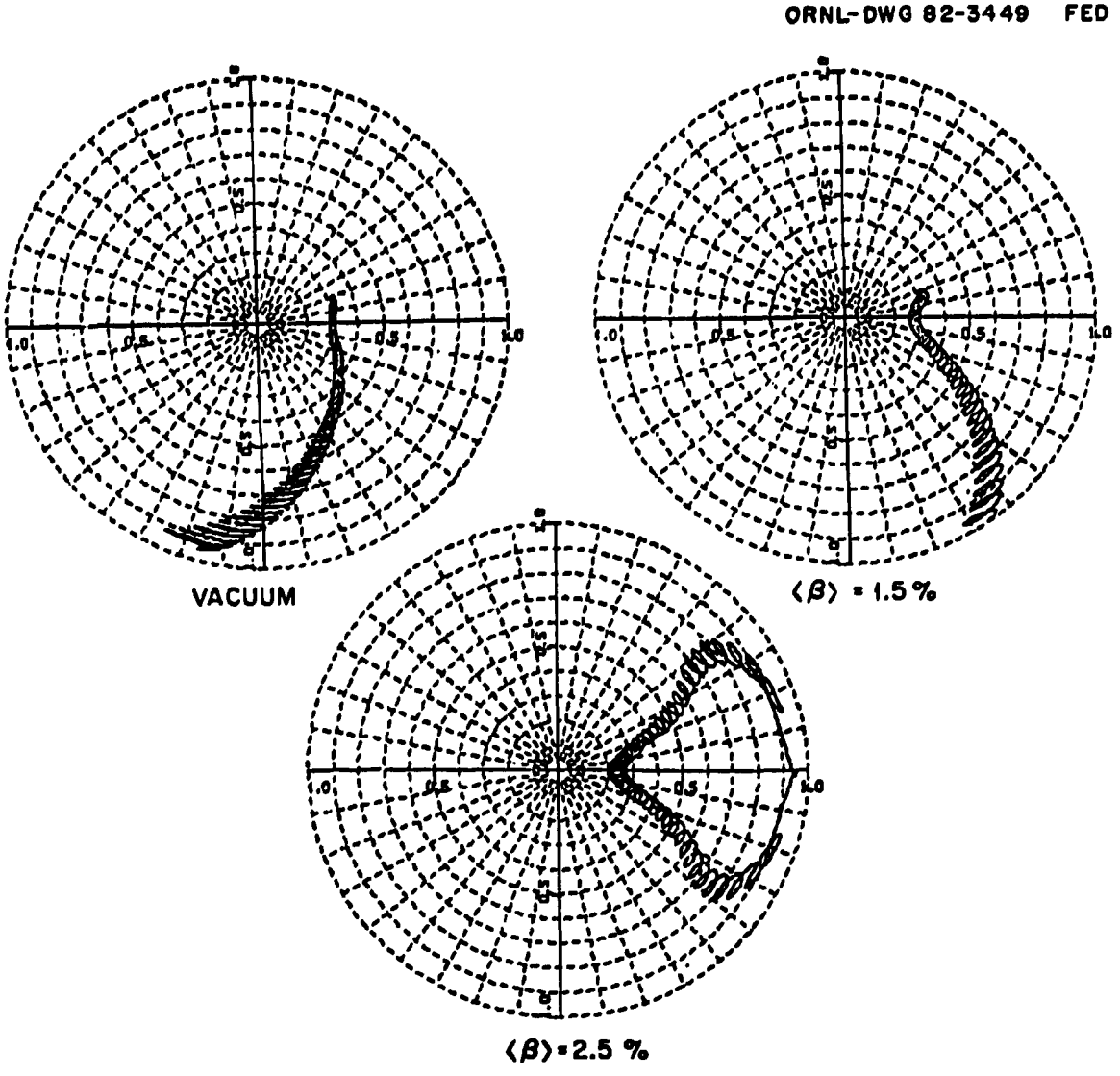

Fig. 5. Effect of beta on orbit topology for a 1-keV, helically trapped proton.

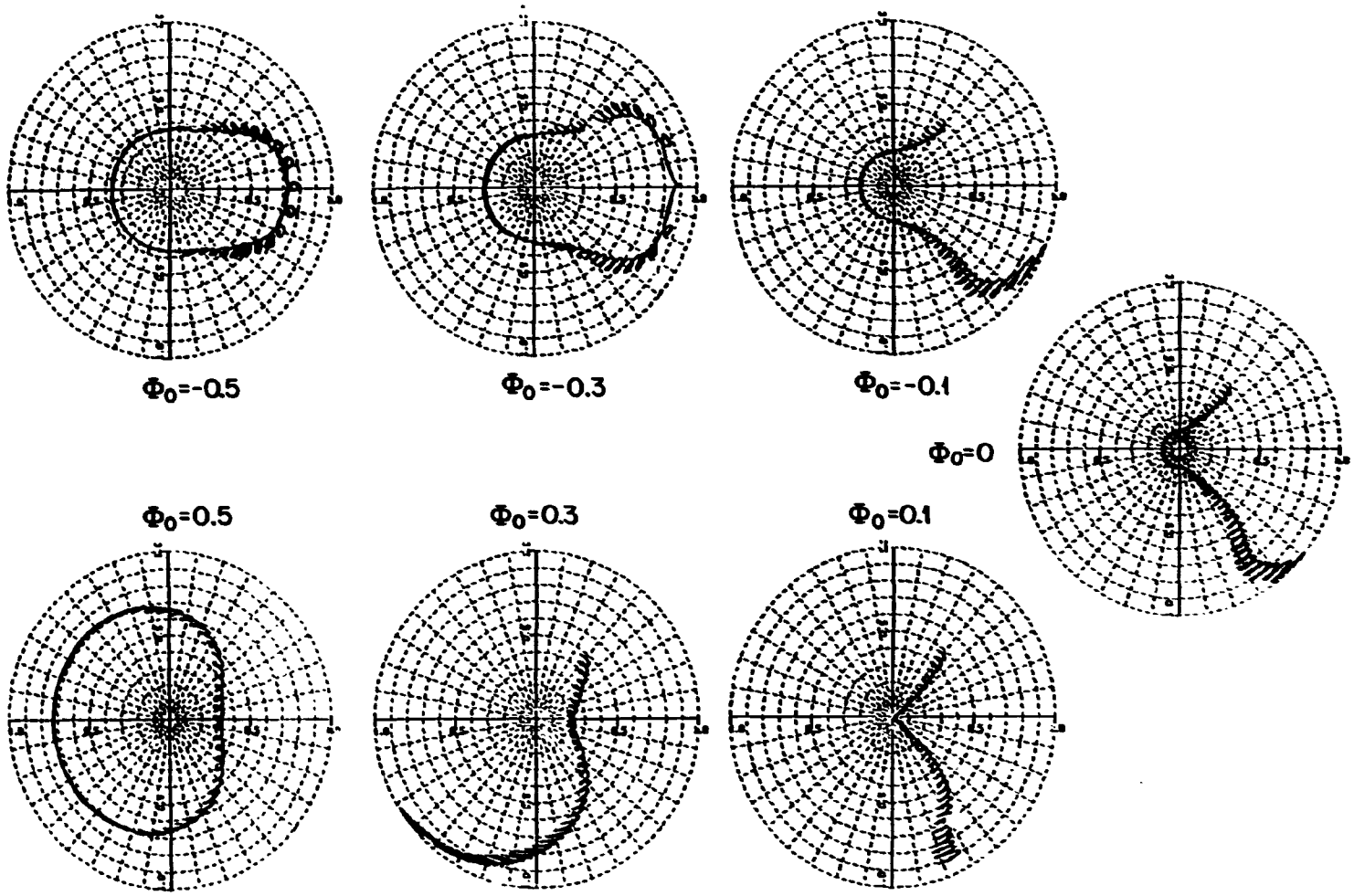

Fig. 6. Effect of radial potential on a 1-keV, helically trapped proton.

helically trapped 1-keV ion in a $\langle\beta\rangle$ = 2.5% equilibrium for various potentials. A positive radial potential yields an $\mathbf{E} \times \mathbf{B}$ velocity in the negative θ direction.

Shaing[11] has derived the particle and heat fluxes in the presence of an electric field in the ν and $1/\nu$ regimes and has joined these regimes together at the resonant transition where $\mathbf{E} \times \mathbf{B}$ and $\mathbf{B} \times \nabla\mathbf{B}$ cancel. An analytic diffusion coefficient is obtained from the resulting expression for the particle flux due to helical trapping, valid for $\epsilon_h >> \epsilon_T$. Figure 7 shows the data points for the Monte Carlo calculations of D in a model $\ell = 1$ stellarator. The parameters are the same as those given for Fig. 1. For small values of the potential, the Monte Carlo results agree closely with the predictions of theory. However, when the potential is increased in magnitude, the value of D rapidly decreases to a residual level, which is roughly the axisymmetric neoclassical values with ν_{ei} replaced by ν_{ii} and m_e replaced by m_i. This asymptotic level is caused by nonconservation of momentum by the Monte Carlo test particles and the resulting flux generated by like-particle collisions. Similar results are obtained when test particles are followed in the correct ATF-1 vacuum field which has a richer harmonic content. These results are given in Fig. 8. The parameters are the same as those given for Fig. 2.

The diffusion coefficients for a finite beta case ($\langle\beta\rangle$ = 2%) are also given in Fig. 8. The magnetic surfaces as calculated from the field obtained by the Chodura-Schlüter code[8] are given in Fig. 9 along with the vacuum magnetic surfaces. Even though there is a shift in the magnetic axis at finite beta, the transport has not been significantly affected.

Figure 10 is the result of a sensitivity study of the number of particles necessary to obtain adequate statistics for the vacuum ATF-1 case. These curves indicate that reasonably accurate diffusion coefficients can be obtained with 256 particles, with the largest errors occurring for the smaller values of the potential.

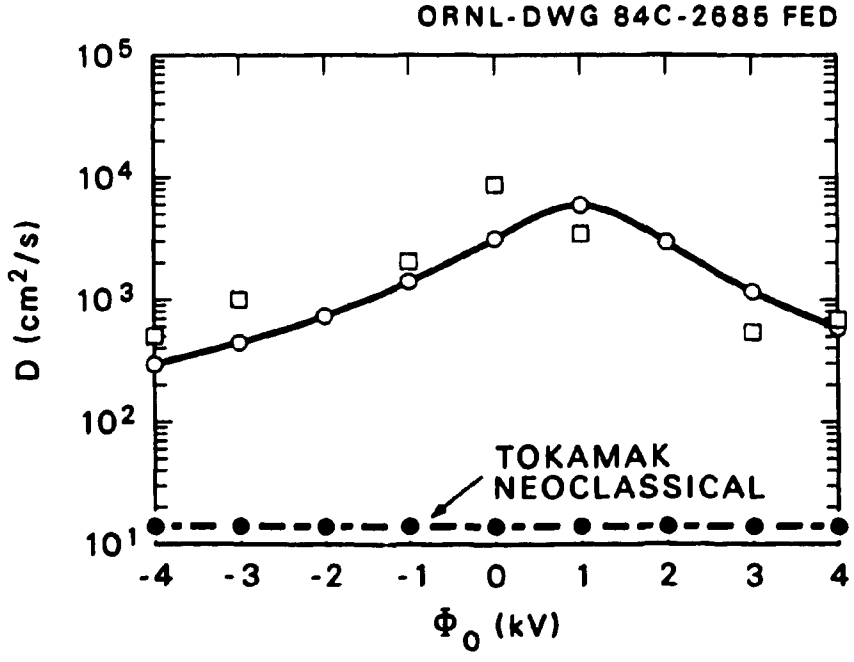

Fig. 7. The diffusion coefficient vs radial potential for a model $\ell = 1$ stellarator with the Monte Carlo results (squares) and the theoretical prediction (solid curve).

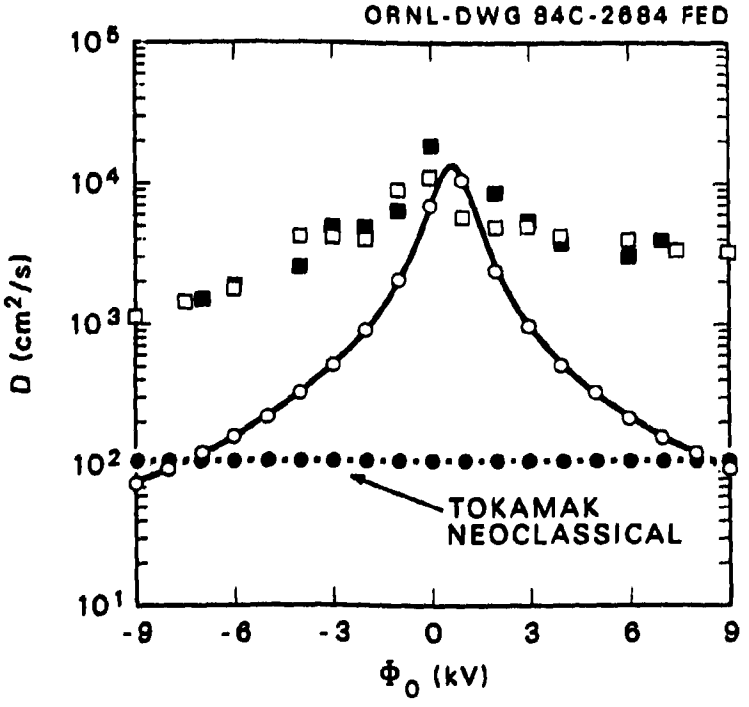

Fig. 8. The Monte Carlo diffusion coefficients vs radial potential for the ATF-1 vacuum field (squares), $\langle\beta\rangle$ = 2% (solid squares), and the theoretical prediction (solid curve).

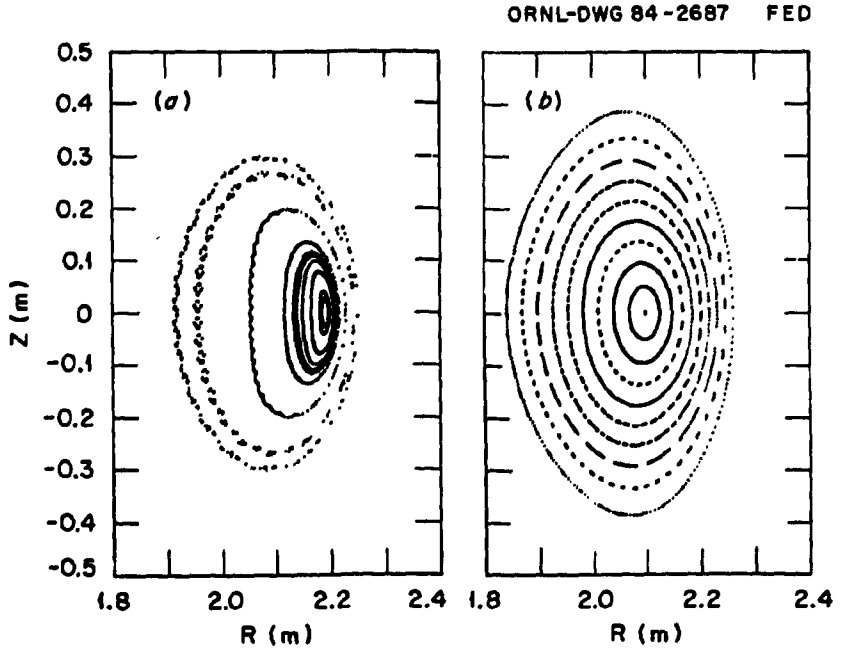

Fig. 9. ATF-1 flux surfaces at ϕ = 0° for (a) $\langle\beta\rangle$ = 2% and (b) vacuum field.

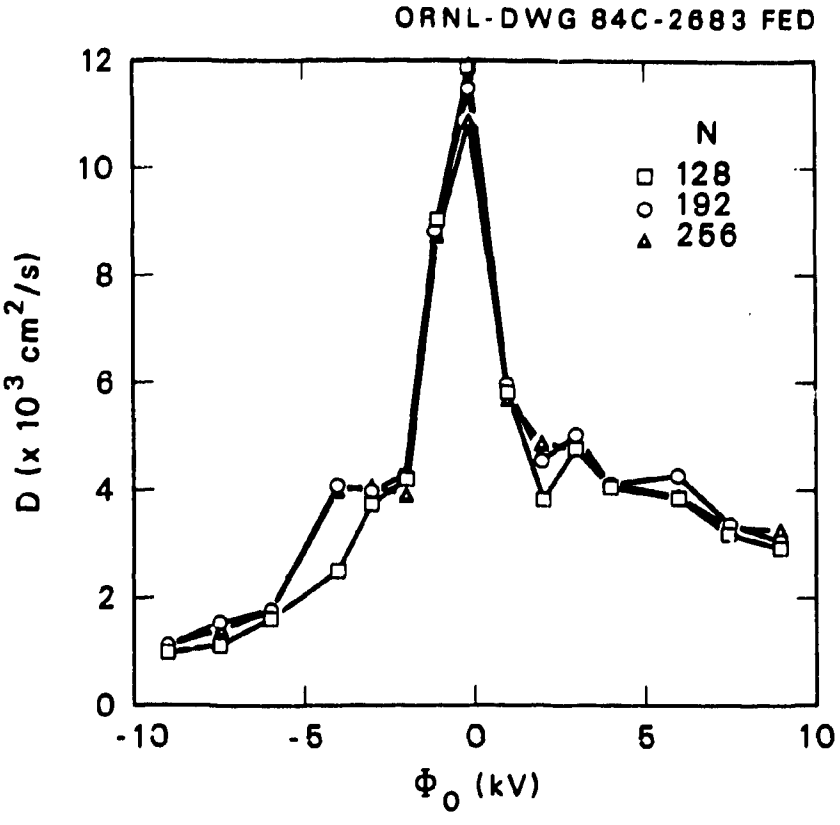

Fig. 10. Numerical sensitivity of the calculation of D on the number of particles.

8. SUMMARY

A Monte Carlo code for computing transport in realistic magnetic fields has been described. The computed diffusion coefficients for a tokamak case compare well with the appropriate analytic theory. The Monte Carlo results for stellarator fields also compare favorably with the theoretical predictions in regimes for which the theory is valid, that is, when diffusion is dominated by helically trapped particles. However, for large electric fields, the asymptotic numerical results are due to nonconservation of momentum of the Monte Carlo test particles. The code is also useful for computing particle and energy loss rates.

ACKNOWLEDGMENTS

The authors wish to acknowledge very useful discussions with W.A.Houlberg, K.C.Shaing, and J.S.Tolliver. Special acknowledgments are due L.Garcia for providing the three-dimensional equilibria and J.L.Cantrell for doing the numerical sensitivity studies.

REFERENCES

1. A. H. Boozer and G. Kuo-Petravic, *Phys. Fluids* **24**, 851 (1981).
2. W. Lotz and J. Nuhrenberg, *Z. Naturforsch* **37a**, 899 (1982).
3. J. Wobig, *Z. Naturforsch* **37a**, 906 (1982).
4. A. H. Boozer, *Time-Dependent Drift Hamiltonian*, IPPJ-571, Institute of Plasma Physics, Nagoya University, Nagoya, Japan, 1982.
5. L. F. Shampine and M. K. Gordon, *Computer Solution of Ordinary Differential Equations*, W. H. Freeman and Company, San Francisco, 1975.
6. R. Bulirsch and J. Stoer, *Numer. Math.* **8**, 1 (1966).
7. G. Kuo-Petravic, A. H. Boozer, J. A. Rome, and R. H. Fowler, *J. Comput. Phys.* **51**, 261 (1983).
8. R. Chodura and A. Schlüter, *J. Comput. Phys.* **41**, 68 (1981).
9. M. N. Rosenbluth, R. D. Hazeltine, and F. L. Hinton, *Phys. Fluids* **15**, 116 (1972).
10. F. L. Hinton and R. D. Hazeltine, *Rev. Mod. Phys.* **48**, 239 (1976).
11. K. C. Shaing, ORNL, private communications.

ORNL/TM-9193
Dist. Category UC-20

INTERNAL DISTRIBUTION

1. L. A. Berry
2. J. L. Cantrell
3. B. A. Carreras
4. L. A. Charlton
5. R. A. Dory
6. J. Dunlap
7–11. R. H. Fowler
12. L. Garcia
13. R. C. Goldfinger
14. J. H. Harris
15. H. H. Haselton
16. H. R. Hicks
17. L. M. Hively
18. J. A. Holmes
19. W. A. Houlberg
20. D. K. Lee
21. V. E. Lynch
22–26. J. F. Lyon
27. R. N. Morris
28. J. K. Munro
29. G. H. Neilson
30. L. W. Owen
31. Y-K. M. Peng
32–36. J. A. Rome
37. M. J. Saltmarsh
38. S. D. Scott
39. K. C. Shaing
40. J. Sheffield
41. D. J. Sigmar
42. D. J. Strickler
43. J. S. Tolliver
44. G. E. Whitesides
45. R. M. Wieland
46-47. Laboratory Records Department
48. Laboratory Records, ORNL-RC
49. Document Reference Section
50. Central Research Library
51. Fusion Energy Division Library
52. Fusion Energy Division Publications Office
53. ORNL Patent Office

EXTERNAL DISTRIBUTION

54. Office of the Assistant Manager for Energy Research and Development, Department of Energy, Oak Ridge Operations, Box E, Oak Ridge, TN 37830
55. J. D. Callen, Department of Nuclear Engineering, University of Wisconsin, Madison, WI 53706
56. R. W. Conn, Department of Chemical, Nuclear, and Thermal Engineering, University of California, Los Angeles, CA 90024
57. S. O. Dean, Director, Fusion Energy Development, Science Applications, Inc., 2 Professional Drive, Gaithersburg, MD 20760
58. H. K. Forsen, Bechtel Group, Inc., Research Engineering, P.O. Box 3965, San Francisco, CA 94105
59. R. W. Gould, Department of Applied Physics, California Institute of Technology, Pasadena, CA 91125
60. D. G. McAlees, Exxon Nuclear Company, Inc., 777 106th Avenue, NE, Bellevue, WA 98009
61. P. J. Reardon, Princeton Plasma Physics Laboratory, P.O. Box 451, Princeton, NJ 08544
62. W. M. Stacey, Jr., School of Nuclear Engineering, Georgia Institute of Technology, Atlanta, GA 30332
63. G. A. Eliseev, I. V. Kurchatov Institute of Atomic Energy, P.O. Box 3402, 123182 Moscow, U.S.S.R.

64. V. A. Glukhikh, Scientific-Research Institute of Electro-Physical Apparatus, 188631 Leningrad, U.S.S.R.
65. I. Spighel, Lebedev Physical Institute, Leninsky Prospect 53, 117924 Moscow, U.S.S.R.
66. D. D. Ryutov, Institute of Nuclear Physics, Siberian Branch of the Academy of Sciences of the U.S.S.R., Sovetskaya St. 5, 630090 Novosibirsk, U.S.S.R.
67. V. T. Tolok, Kharkov Physical-Technical Institute, Academical St. 1, 310108 Kharkov, U.S.S.R.
68. R. Varma, Physical Research Laboratory, Navrangpura, Ahmedabad, India
69. Bibliothek, Max-Planck Institut fur Plasmaphysik, D-8046 Garching bei Munchen, Federal Republic of Germany
70. Bibliothek, Institut fur Plasmaphysik, KFA, Postfach 1913, D-5170 Julich, Federal Republic of Germany
71. Bibliotheque, Centre de Recherches en Physique des Plasmas, 21 Avenue des Bains, 1007 Lausanne, Switzerland
72. Bibliotheque, Service du Confinement des Plasmas, CEA, B.P. 6, 92 Fontenay-aux-Roses (Seine), France
73. Documentation S.I.G.N., Departement de la Physique du Plasma et de la Fusion Controlee, Centre d'Etudes Nucleaires, B.P. No. 85, Centre du Tri, 38041 Cedex, Grenoble, France
74. Library, Culham Laboratory, UKAEA, Abingdon, Oxfordshire, OX14 3DB, England
75. Library, FOM Institut voor Plasma-Fysica, Rijnhuizen, Jutphaas, The Netherlands
76. Library, Institute of Physics, Academia Sinica, Beijing, Peoples Republic of China
77. Library, Institute of Plasma Physics, Nagoya University, Nagoya 64, Japan
78. Library, International Centre for Theoretical Physics, Trieste, Italy
79. Library, Laboratorio Gas Ionizzati, Frascati, Italy
80. Library, Plasma Physics Laboratory, Kyoto University, Gokasho Uji, Kyoto, Japan
81. Plasma Research Laboratory, Australian National University, P.O. Box 4, Canberra, A.C.T. 2000, Australia
82. Thermonuclear Library, Japan Atomic Energy Research Institute, Tokai, Naka, Ibaraki, Japan

83–189. Given distribution as shown in TID-4500, Magnetic Fusion Energy (Distribution Category UC-20)